Mon. Not. R. Astron. Soc. **000**, 000–000 (0000) Printed 25 July 2008 (MN LaTeX style file v2.2)

Quantifying mass-loss rate and wind porosity using the X-ray emission line profiles of ζ Puppis

David H. Cohen,[1*] Maurice A. Leutenegger,[2] Emma E. Wollman,[1]
Stanley P. Owocki,[3] Richard H. D. Townsend[3,4]
[1] *Swarthmore College, Department of Physics and Astronomy, Swarthmore, Pennsylvania 19081, USA*
[2] *NASA/Goddard Space Flight Center, Laboratory for High Energy Astrophysics, Code 622, Greenbelt, Maryland 20771, USA*
[3] *University of Delaware, Barol Research Institute, Newark, Delaware 19716, USA*
[4] *University of Wisconsin, Department of Astronomy, Madison, 475 N. Charter St., Madison, Wisconsin 53706, USA*

25 July 2008

ABSTRACT

We fit X-ray line profile models, including the effects of large-scale wind porosity, to the high-resolution *Chandra* spectrum of the O4 supergiant ζ Pup. We find that models that include porosity provide a somewhat worse fit to the data than models where the X-ray opacity is purely atomic and which do not include porosity. We also fit a porous model with oblate clumps, and find that it provides much worse fits to the data. From the fits to 14 emission lines between 6 and 22 Å we find a modest wavelength dependence in the optical depth, which is consistent with the expected atomic opacity and inconsistent with a porosity dominated medium, where the geometrical cross section of the clumps governs the effective opacity. From the fits to these lines, we derive a mass-loss rate of 3.0×10^{-6} $M_{\odot}$ yr^{-1}, which represents a factor of ~ 3 reduction of the traditional mass-loss rate derived assuming no wind clumping.

Key words: stars: early-type – stars: mass-loss – stars: winds, outflows – stars: individual: ζ Pup – X-rays: stars

1 INTRODUCTION

The dense and highly supersonic radiation-driven winds of O stars are generally supposed to be the site of X-ray production in these massive stars. Broadened X-ray emission line profiles ($v_{hwhm} \approx 1000$ km s^{-1}), first measured with *XMM-Newton* and *Chandra* early in this decade, provide direct evidence for hot plasma kinematics consistent with the same beta velocity law that describes the bulk of the cool ($T < T_{\rm eff}$) wind (Kramer et al. 2003). The hot, X-ray emitting plasma is thought to be produced by shock heating of a small fraction of the wind to temperatures of a few million K, and it is generally supposed that the line-driven intability (LDI) is the cause of the shocks (Owocki et al. 1988; Feldmeier et al. 1997; Dessart & Owocki 2003). The high-resolution X-ray spectra not only provide information about the hot, X-ray emitting wind component, they also provide important information about the bulk, cool wind component which attenuates the emitted X-rays.

The early O supergiants, with the highest mass-loss rates, are expected to have winds that are quite optically thick to X-rays (Hillier et al. 1993). One readily observable effect of optically thick winds is the apparent blue shift and asymmetry of emission lines, which arises because red shifted X-rays emitted from the back of the wind are preferrentially absorbed compared to blue shifted photons from the front hemisphere of the wind. The degree of blue shift and asymmetry is proportional to a single paramter that describes the optical depth along the central ray, $\tau_* \equiv \frac{\dot{M}\kappa}{4\pi R_* v_\infty}$. So, the line profile shape, through τ_*, provides a powerful diagnostic of the mass-loss rate.

The wind optical depth also depends on the opacity, which is generally assumed to be due to photoelectric absorption from metals,and has a modest wavelength dependence. The level and detailed form of this opacity requires knowledge of the star's abundances and the ionization state of its wind. It has been shown, though, that large-scale clumping can reduce the effective opacity (Feldmeier et al. 2003; Oskinova et al. 2004, 2006; Owocki & Cohen 2006). This effect only occurs once individual clumps become optically thick (Owocki & Cohen 2006), so that opacity can be effectively hidden in the interior of clumps. When this criterion is met, we say that the wind is porous; photon escape

* E-mail: cohen@astro.swarthmore.edu

from the wind is enhanced by this porosity; and the wind's effective opacity is reduced. Note that small-scale clumping (so-called microclumping) as well as large-scale macroclumping, will affect density squared mass-loss diagnostics regardless of the clump scale and clump optical thickness. But only macroclumping will make the medium porous and actually reduce the effective opacity of the wind. The key parameter to describe the effects of porosity on X-ray line profiles is the porosity length, $h \equiv \ell/f$, where ℓ is the characteristic clump size scale and f is the volume filling factor of clumps (the interclump medium is assumed to contain negligible mass). In the limit of completely optically thick, geometrically thin clumps ("shell fragments" in the parlance of Feldmeier et al. (2003)), the porosity length is also the photon mean free path in the radial direction, or the radial interclump spacing.

The lower than expected optical depths derived from the measured X-ray line profiles of O stars imply some combination of reduced mass-loss rates and porosity associated with large-scale wind clumping. In principle, the observed X-ray profiles can be used to derive mass-loss rates of O stars that are independent of the traditional H-alph, radio free-free excess, and UV absorption line diagnostics of mass loss, many of which have recently shown that O star mass-loss rates are lower than previously assumed. However, it has also recently been claimed that the mass-loss rates of O stars do not need to be revised downward and instead that the only modestly shifted and asymmetric profiles are instead evidence of large scale porosity in the structure of O star winds (Oskinova et al. 2006). But until now, no quantitative analysis has been done on the available high-resolution X-ray spectra of O stars, which can discriminate between the effects of mass-loss rate reduction and porosity and explore the quantitative trade-offs between these two effects.

The effects of mass-loss rate reduction (or a reduction in atomic opacity) are different from that of porosity, in terms of the specific profile shape produced. In this paper, we directly test the two different effects – mass-loss rate reduction and porosity – with high-resolution *Chandra* grating spectrum of the canonical O supergiant ζ Pup. We do this by fitting simple, empirical line profile models that include the two key parameters that are controlled by the mass-loss rate (τ_*) and by the degree of porosity (h_∞), respectively, to the profiles in the *Chandra* HETGS spectrum of ζ Pup. We examine the confidence limits on these two parameters and address the following two questions: (1) Are models with porosity preferred to models without porosity? And (2) to the extent that we cannot say which type of model – porous or non-porous – is preferred from fitting a given line, what quantitative limits can be put on the amount of porosity required to provide adequate fits to the data given the expected mass-loss rate of this O supergiant? As we systematically address these two questions, we will also re-evaluate the optical depths derived from non-porous fits to individual line profiles and, using detailed models of the wind opacity, derive a mass-loss rate for ζ Pup that is consistent with the X-ray data (assuming that porosity is not important, which is what the fits of profile models that include porosity indicate). We also introduce a modified X-ray line profile model that accounts for non-spherical clumps, and show that it does not provide better fits to the profile than the porosity model that assumes spherical clumps. And finally, we explore the implications of the wavelengh dependence of the line profile shapes, and see that the observed wavelength dependence is consistent with atomic opacity, rather than porosity, governing the radiation transport properties of X-rays in the wind of ζ Pup.

We begin by describing the *Chandra* data set and defining a sample of well behaved emission lines for our analysis in §2. We also briefly evaluate the stellar and wind properties of ζ Pup in this section. In §3 we provide a framework for describing wind clumping and present a simple means of parameterizing the effects of the porosity that can be associated with large-scale clumping. And we briefly show how porosity affects X-ray emission line profiles. In §4 we describe our procedure for analyzing data with the line-profile models presented in the previous section. In §5 we present our results, and in §6 we discuss their implications, including a consideration of wavelength-dependent wind opacity and the results of state-of-the-art two-dimensional radiation hydrodynamics simulations of wind structure induced by the line-driven instability. In §7 we conclude that the line profile shapes in the *Chandra* grating spectrum of ζ Pup require a mass-loss rate of 3.0×10^{-6} $M_\odot$ yr^{-1}, and that higher mass-loss rates can be accommodated if the effective optical depth of the wind is reduced by porosity, but that unrealistically large values of the porosity length are required for consistency with the literature mass-loss rates. We also conclude that the wavelength dependence of the profile properties is consistent with mass-loss rate reduction and not with the gray effective opacity implied by significant porosity effects.

2 THE *Chandra* GRATING SPECTRUM OF ζ Pup

2.1 The data

All the data we use in this paper was taken on 28-29 March 2000 in a single, 68 ks observation using the *Chandra* High-Energy Transmission Grating Spectrometer (HETGS) in conjunction with the Advanced CCD Imagine Spectrometer (ACIS) detector in spectroscopy mode. This is a photon counting instrument with an extremely low background and high spatial resolution ($\approx 1''$). The first-order grating spectra we analyze have a total of 21,684 counts, the vast majority of which are in emission lines, as can be seen in Fig. 1. We modeled every line the two spectra, as we describe in §4 and §5, and indicate in this figure which of the lines we deemed to be reliable (strong and unblended enough for the uncertainties in the derived parameter values to be dominated by statistical noise).

The HETGS assemply has two grating arrays - the Medium Energy Grating (MEG) and the High Energy Grating (HEG) - with spectral resolutions of 0.0023 Å and 0.0012 Å, respectively. This corresponds to a resolving power of $\mathcal{R} \approx 1000$, or a velocity of 300 km s^{-1}, at the longer wavelength end of each grating. The wind-broadened X-ray lines of ζ Pup are observed to have $v_{\rm fwhm} \approx 2000$ km s^{-1}, and so are very well resolved by *Chandra*. The wavelength calibration of the HETGS is accurate to 50 km s^{-1}.

The two gratings, detector, and telescope assembly have significant response from roughly 2 Å to 30 Å, with typical effective areas of tens of cm^2, and a strong function of wavelength. In practice, the shortest wavelength line with significant flux in the relatively soft X-ray spectra of O stars like ζ Pup is the Si XIV Lyman-alpha line at 6.182 Å, and the longest wavelength line is the N VII Lyman-alpha line at 24.781 Å. The HEG response is negligible for lines with wavelengths longer than about 16 Å.

The X-ray spectrum of ζ Pup consists primarily of emission lines from H-like and He-like ionization stages of N, O, Ne, Mg, and Si, and numerous L-shell lines of iron, primarily Fe, XVII. The Lyα lines and often the β and even γ lines of the Lyman series are seen for the H-like ions. The Heα complexes consist of three lines, the resonance, intercombination (i), and forbidden (f). The f/i ratio is sensitive to the local UV mean intensity, and thus to the distance the X-ray emitting plasma is from the UV emitting photosphere. The components of these complexes are blended; and quite severely so for the shorter wavelength (higher Z) elements. There is a weak bremsstrahlung continuum beneath these lines. Overall, the spectrum is consistent with an optically thin, thermal plasma in ionization equilibrium with a range of temperatures from one to several million degrees present. It is possible that there are deviations from equlibrium, although the spectrum is not of high enough quality to show this, and there is some evidence from the *XMM-Newton* RGS spectrum that a few of the emission lines are optically thick (Leutenegger et al. 2007). We fit every identifiable line in the spectrum, but ultimately only include lines in our analysis that are not so weak or severely blended that interesting parameters of the line-profile models cannot be constrained.

2.2 The star

ζ Puppis is nearby ($d = 335^{+12}_{-11}$ pc)[1], single, runaway early O supergiant that shows the enhanced nitrogen and deficient oxygen that is indicative of CNO cycle processed material. Its rapid rotation may explain the photospheric abundance anomalies, though it has also been claimed that it had a close binary companion that exploded as a supernova, rendering it a runaway and perhaps explaining its abundances. Detailed spectral synthesis has been carried out from the UV to the IR to determine the stellar and wind properties of ζ Pup, which we list in Table 1. Most of these are taken from Puls et al. (2006). There is a range of wind property determinations in the extensive literature on ζ Pup. The terminal velocity of the wind may be as low as 2100 km s^{-1}, and as high as 2485 km s^{-1}. Mass-loss rate determinations vary as well, partly because of the uncertainty in the distance, but also because each mass-loss rate diagnostic is subject to uncertainty: density squared diagnostics like Hα and free-free emission are affected by clumping, no matter the size scale and optical depth of the clumps (so, micro-clumping). Mass-loss rates from UV absorption lines are subject to uncertain ionization corrections. In the last few years, micro-clumping

Table 1. Stellar and wind parameters adopted from Puls et al. (2006)

parameter	value
Sp. Type	O4 If
Mass^a	53.9 M$_\odot$
$T_{\rm eff}$	39000 K
R$_*$	18.6 R$_\odot$
$v_{\rm rot}\sin i$	–
v_∞	2250 km s^{-1}
β	0.9
$\dot{M}^b$	8.3×10^{-6} M$_\odot$ yr^{-1}
$\dot{M}^c$	4.2×10^{-6} M$_\odot$ yr^{-1}
$\dot{M}^d$	1.5×10^{-6} M$_\odot$ yr^{-1}

[a] From Repolust et al. (2004).
[b] Unclumped value from Puls et al. (2006).
[c] Also from Puls et al. (2006), but the minimum clumping model, in which the far wind, where the radio emission arises, is unclumped.
[d] From Bouret et al. 2008, assuming clumping.

has started to be taken into account when deriving mass-loss rates from both density-squared diagnostics and UV absorption diagnostics. We list several mass-loss rate determinations in the table, with notes about the assumptions behind each determination. The X-ray line profile diagnostics of mass-loss rate that we employ in this paper are not directly affected by micro-clumping; only by macro-clumping and the associated porosity[2]

The star shows periodic variability in various UV wind lines as well as H$_\alpha$. Its broad-band X-ray properties are normal for an O star, with $L_{\rm x} \approx 10^{-7} L_{\rm Bol}$ and a soft spectrum, dominated by optically thin thermal line and free-free emission from plasma with a temperature of a few million degrees. The emission measure filling factor of the wind is small, roughly one part in 10^3. Weak soft X-ray variability, with an amplitude of 6 percent, and a period consistent with the 18 hr H$_\alpha$ period, was detected with *ROSAT*. This low-level variability appears not to affect the *Chandra* data.

[1] The original Hipparcos distance determination had rather large error bars; this value is from a recent reanalysis of the data. The derived stellar parameters and mass-loss rate depend on the distance. And the distance also has implications for the origin of ζ Pup.

[2] Though, of course, the X-ray profiles are affected by mass-loss rate re-evaluations that take micro-clumping into account.

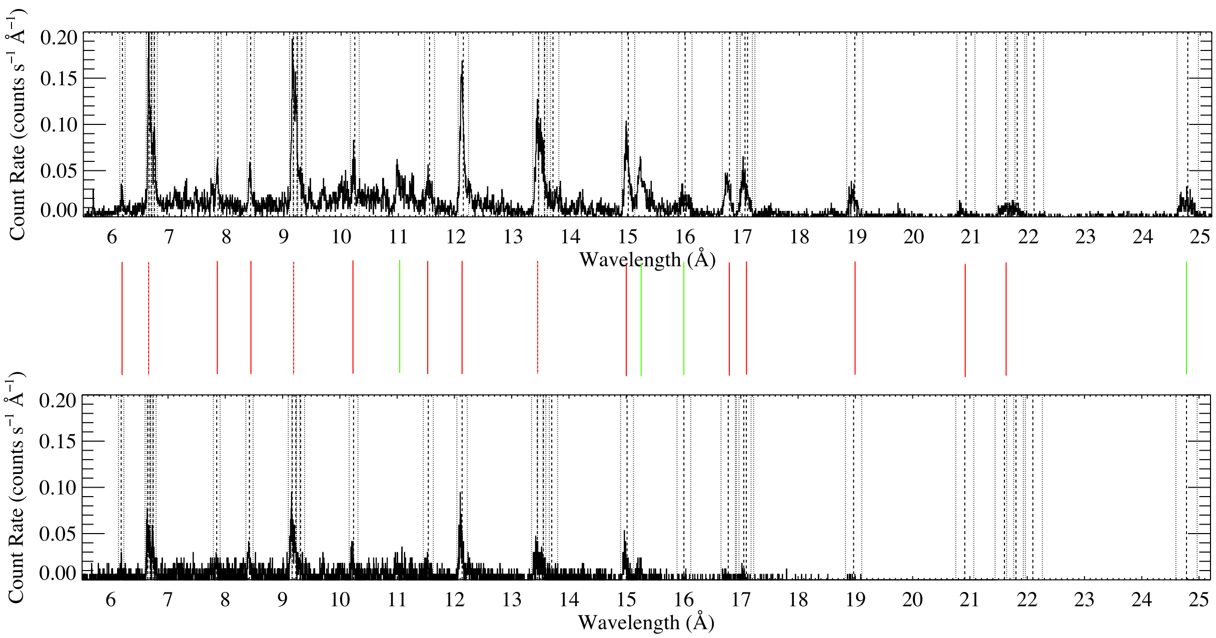

Figure 1. The entire usable portions of the MEG (top) and HEG (bottom) first order spectra of ζ Pup. The binning is native (2.5 mÅ for the HEG and 5 mÅ for the MEG). Vertical dashed lines in the data panels themselves represent the laboratory rest wavelengths of important lines. The lighter dotted lines on either side represent the Doppler shifts associated with the star's terminal velocity. Bold vertical lines between the two spectral plots indicate the lines we successfully fit with profile models (solid red) and lines we attempted to fit but which were too blended to extract meaningful model parameters (solid green). The helium-like triplets are indicated by dotted lines.

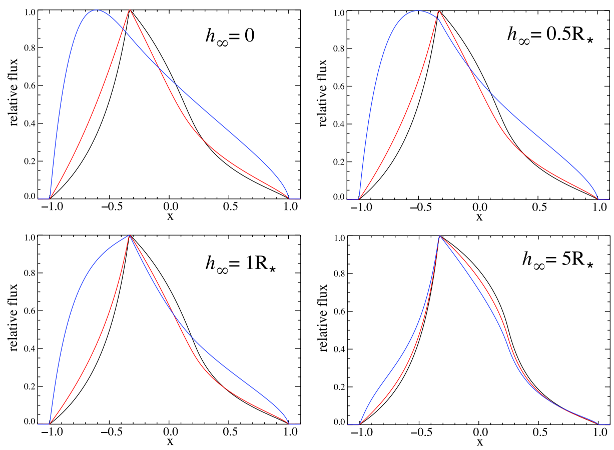

Figure 2. Line profile models that incorporate isotropic porosity. Each panel shows profiles with $R_{\rm o} = 1.5$ R$_*$ and three different values of τ_*, $\tau_* = 1, 2, 8$. The terminal porosity length increases from zero in the top left panel (so, these models are non-porous) to $h_\infty = 5$ R$_*$. Note that the effects of porosity are not significant until the porosity length is of order the stellar radius.

3 THE EMISSION LINE PROFILE MODEL AND POROSITY

4 ANALYSIS AND MODEL-FITTING PROCEEDURE

4.1 Demonstration with one representative emission line

For each line in the spectrum, we first attempt to fit the non-porous (Owocki & Cohen 2001) profile model, described by equations **??** and **??**, to the data. Note that this model has only three free parameters: the fiducial optical depth, τ_*, the minimum radius of X-ray emission, R_o, and the normalization of the line. After this, we fit the porous model with spherical clumps (Owocki & Cohen 2006), and lastly we fit the porous model with flattened clumps. These two porous models each have only one additional free parameter, the terminal porosity length, h_∞, described by equation **??**.

We begin the analysis proceedure for each line by fitting the weak continuum in two regions, one on the blue side of the line and one on the red side. We assume the continuum is flat over this restricted wavelength region. We then fit the emission line over a wavelength range that is no broader than the line itself (and sometimes even narrower, due to blends with nearby lines, which induce us to exclude contaminated portions of the line in question). The model we fit to each line is the sum of the empirical line profile model(s) we described in the previous section and the continuum model determined from the fit to the two spectral regions near the line. Note though that the inclusion of the continuum does not introduce any new free parameters.

We fit the wind profile plus continuum model to both the MEG and HEG data (positive and negative first orders) simultaneously, if the HEG data are of good enough quality to warrant their inclusions (generally true only for lines shorter than about 16 Å), and to the MEG data only if they are not. We use the C statistic as the goodness of fit statistic. This is the maximum likelihood statistic for data with Poisson distributed errors, which our photon-counting X-ray spectra are. Note that the maximum likelihood statistic for Gaussian distributed data is the well-known χ^2 statistic, but it is not valid for these data, which have many bins with only a few counts, especially in the diagnostically powerful wings of the profiles.

We determine the best-fit model by minimization of the C statistic using the *fit* task in XSPEC. Once it is found, the uncertainties on each model parameter are assessed using the $\Delta\chi^2$ formalism outlined in (Press et al., Ch. 16), which is also valid for ΔC[3]. We test each parameter one at a time, stepping through a grid of values and, at each step, refitting data while letting the other model parameters be free to vary. The 68 percent confidence limits determined in this manner are what report as the formal uncertainties in the tables of fitting results in the next section. We also examine the confidence regions in two-dimensional sub-spaces of the whole parameter space, in order to look for correlations among the interesting parameters.

We will use the relatively strong and unblended Fe XVII line at 15.014 Å to demonstrate this fitting process. We show the MEG and HEG data for this line, along with the best-fit model (the set of model parameters, τ_*, R_o, and normalization which mimimizes the C statistic) in Fig. 3. The best-fit parameters for this model fit are: $\tau_* = 1.97$, $R_o = 1.53$ R_*, and a normalization of 5.24×10^{-4} photons s^{-1} cm^{-2}. Using the ΔC criteron and testing each of these parameters one at a time, we find that the 68 percent confidence limits on the fit parameters are $1.63 < \tau_* < 2.35$, $1.38 < R_o < 1.65$, and $5.04 \times 10^{-4} <$ norm $< 5.51 \times 10^{-4}$.

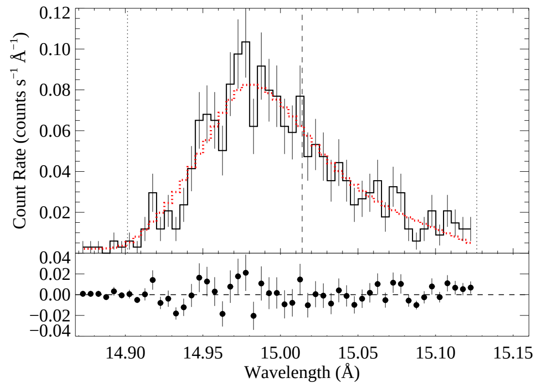

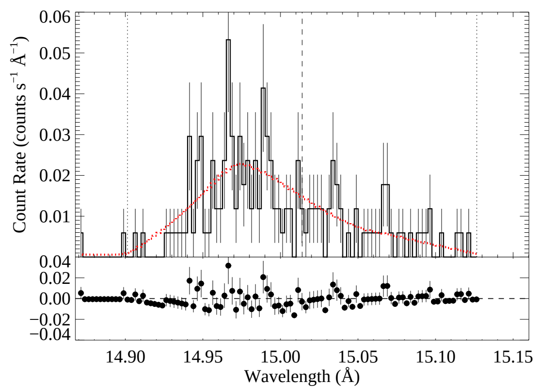

Figure 3. The Fe XVII line at 15.014 Å in the MEG (top) and HEG (bottom), with the best-fit non-porous model superimposed. We have not done any rebinning of the data. The error bars represent Poisson, root-N, statistics. The dashed vertical line indicates the laboratory rest wavelength of the line, and the two dotted vertical lines indicate the wavelengths associated with the Doppler shift due to the stellar wind terminal velocity of 2250 km s^{-1}. The model is shown as a (red) smooth histogram, while the data are shown as a (black) choppy histogram with error bars. The fit residuals are shown in the horizontal windows below the data.

In Fig. 4 we show 68, 90, and 95 percent confidence limits in two-dimensional τ_*, R_o parameter space. We calculate a 35 by 35 grid of models, optimizing the other free parameters (just the normalization, in this case) at each point in the grid), and use values of $\Delta C = 2.30, 4.61, 6.17$ to define the extent of the confidence limits. Plots such as this one are a good means of examining correlations between model parameters, in terms of their abilities to produce similar features in the line profiles. We can see what the tradeoffs are between parameters in a quantitative way. For example, there is a slight correlation between u_o and τ_* evident in the figure. High values of u_o (R_o close to R_*), reduce emis-

[3] This criterion is a specific numerical value of $\Delta C \equiv C_i - C_{min}$ for model realization i, where $C_{\rm min}$ is the C statistic value for the best-fit model.

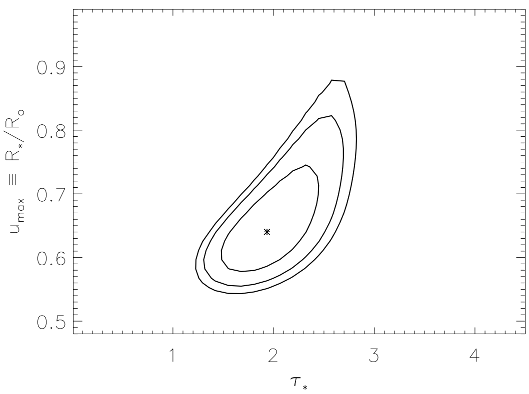

Figure 4. Confidence contours (68, 90, and 95 percent) for the non-porous model fitting of the the Fe XVII line at 15.014 Å. The best-fit, shown in Fig. 3, is represented by the asterisk. Note that we plot this, and all other confidence plots that involve the inner radius, R_o, in terms of $u_o \equiv R_*/R_o$.

sion on the line wing relative to the core (more emitting material at low velocity). So although high values of u_o (hot plasma as close as 1.2 R_*) are allowed at the 95 percent confidence limit, they require large wind optical depth, $\tau_* \approx 3$, to compensate. High τ_* makes lines more blue-shifted and asymmetric, increasing the emission on the line wing relative to the core.

The value of τ_* expected from the traditional mass-loss rate and a model of the wind opacity at 15 Å, is $\tau_* \approx 7$. The best-fit model with $\tau_* = 7$ is shown in Fig. 5. This model does not provide a good fit, having $\Delta C = 108$.

After fitting the non-porous, Owocki & Cohen (2001) line profile model, we next fit a given emission line with the model that includes porosity from spherical clumps (Owocki & Cohen 2006), as given by equation **??**.This introduces an additional free parameter, h_∞. We repeat the process described above, finding the best-fit model by minimizing the fit statistic, assessing confidence limits on parameters individually and then examining joing confidence limits on pairs of parameters.

For the Fe XVII line at 15.014 Å, we found that $h_\infty = 0.0$ was the best-fit value of the terminal porosity length. This is equivalent to a model without porosity . The 68 percent confidence limit on this value is $h_\infty = 0.43$ R_* and the 90 percent confidence limit is $h_\infty = 1.07$ R_*. We can examine how this parameter interacts with the optical depth parameter, τ_*. In Fig. 6 we show the confidence contours in two-dimensional h_∞, τ_* parameter space. The correlation seen here between h_∞ and τ_* arises from the ability of porosity to reduce the effective opacity of the wind, by hiding atomic opacity in optically thick clumps. And just as is expected theoretically (Owocki & Cohen 2006), the effect only becomes significant once the porosity length is is equivalent to the local radius (here, roughly 1.5 R_* and above, based on the fitted value of R_o). The confidence contours, enclosing parameter values that provide acceptable fits, show increasing correlation as h_∞ increases, but the effect of porosity on τ_* does not become significant until h_∞ is above 1 R_*.

We have already shown that models with $\tau_* = 8$, the value implied by the traditional mass-loss rate, provide poor

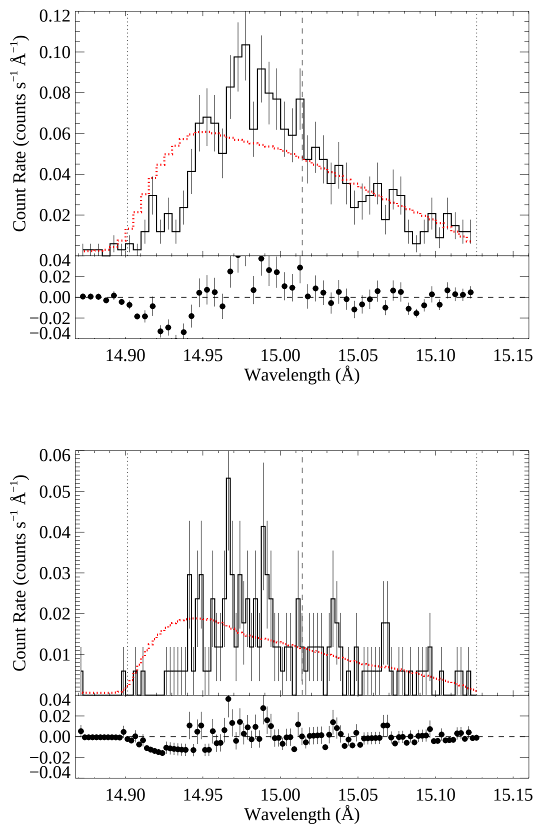

Figure 5. The Fe XVII line at 15.014 Å in the MEG (top) and HEG (bottom), with the best-fit non-porous model having $\tau_* = 7$ superimposed.

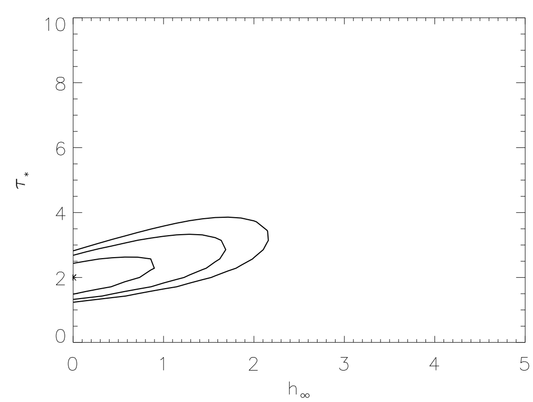

Figure 6. Confidence contours (68, 90, and 95 percent) for the porous model fitting of the the Fe XVII line at 15.014 Å.

fits to this line. And even the 95 percent confidence region in the porous model fitting does not enclose any models with $\tau_* = 8$. However, we can still ask how large a value of h_∞ is required to accomodate this high value of τ_* expected from the traditional mass-loss rate. When we fit a model with $\tau_* = 8$ fixed and porosity included to reduce the effective optical depth of the wind, we find a best-fit value for the terminal porosity length of $h_\infty = 3.64$ R_*. We show this

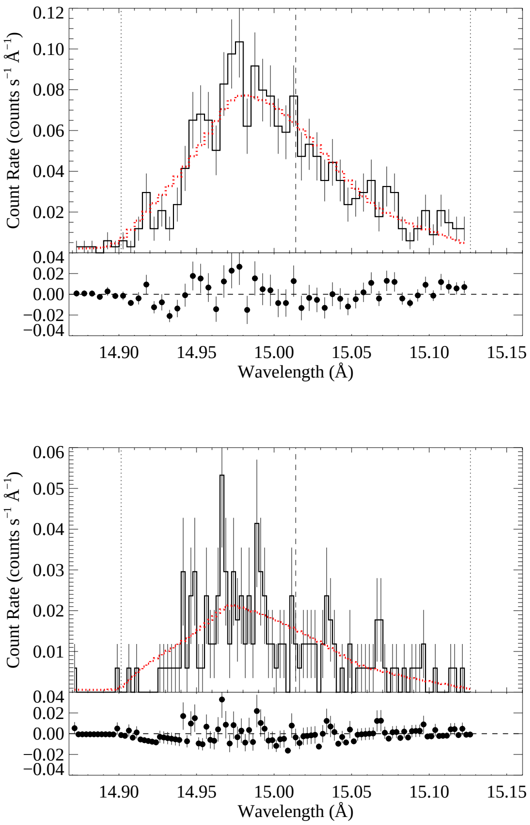

Figure 7. The Fe XVII line at 15.014 Å in the MEG (top) and HEG (bottom), with the best-fit non-porous model having $\tau_* = 7$ superimposed. Compare to Fig. 3.

high τ_*, high h_∞ model in Fig. 7. Although this model cannot be rejected outright, it provides a worse fit to the data than does the non-porous model. The ΔC between these two models is $\Delta C \approx 15$, indicating that the non-porous model is preferreed at the 99.9 percent confidence level. In other words, if the best-fit non-porous model is the correct model, that completely describes the data, then there is only a 0.1 percent chance that a fit as poor as (*e.g.* with the same C statistic as) the one provided by the best-fit porous model due to random error. And this model does have a noticeable bulge on the extreme blue wing as well as one near line center, which is where the agreement is the worst.

4.2 Sensitivity of fitting results to modeling assumptions

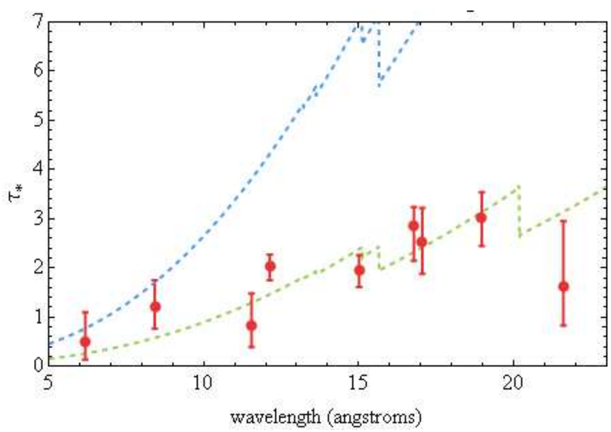

Figure 8. Values of τ_* derived from the non-porous model fits, shown as points with error bars. The value of τ_* expected from the literature mass-loss rate of 8.3×10^{-6} $M_\odot$ yr^{-1} is shown in blue. Treating the mass-loss rate as a free parameter, the best fit value of 3.0×10^{-6} $M_\odot$ yr^{-1} is shown in green.

5 RESULTS OF THE LINE PROFILE MODEL FITTING

6 DISCUSSION AND IMPLICATIONS OF RESULTS

7 CONCLUSIONS

ACKNOWLEDGMENTS

We thank...AR7-8002X...

REFERENCES

Dessart L., Owocki S. P., 2003, A&A, 406, L1

Feldmeier A., Oskinova L., Hamann W.-R., 2003, A&A, 403, 217

Feldmeier A., Puls J., Pauldrach A.W.A., 1997, A&A, 322, 878

Hillier D. J., Kudritzki R.–P., Pauldrach A. W. A., Baade D., Cassinelli J. P., Puls J., Schmitt J. H. M. M., 1993, ApJ, 276, 117

Kramer R. H., Cohen D. H., Owocki S. P., 2003, ApJ, 592, 532

Leutenegger M. A., Paerels F. B. S., Kahn S. M., Cohen D. H., 2006, ApJ, 650, 1096

Leutenegger M. A., Owocki S. P., Paerels F. B. S., Kahn S. M., 2007, ApJ, 659, 642

Oskinova L., Feldmeier A., Hamann W.-R., 2004, A&A, 422, 675

Oskinova L., Feldmeier A., Hamann W.-R., 2006, MNRAS, 372, 313

Owocki S.P., Castor J.I., Rybicki G.B., 1988, ApJ, 335, 914

Owocki S.P., Cohen D.H., 2001, ApJ, 559, 1108

Owocki S.P., Cohen D.H., 2006, ApJ, 648, 565

Puls J., Markova N., Scuderi S., Stanghellini C., Taranova O. G., Burnley A. W., Howarth I. D., 2006, A&A, 454, 625

Repolust T., Puls J., Herrero A., 2004, A&A, 415, 349